DFT calculation of the Renner Teller Effect in NCO: Preliminary assessment of Exact Exchange Energy on the accuracy of the $X^2\Pi$ Renner Coefficient

David O. Kashinski[1]* | **Tyler J. Radziewicz**[1] |
Matthew G. Suarez[1] | **Constantine C. Stephens**[1] |
Edward F. C. Byrd[2]

[1]Department of Physics and Nuclear Engineering, United States Military Academy, West Point, NY, 10996, USA

[2]Weapons and Materials Research Directorate, Army Research Laboratory, Aberdeen Proving Ground MD, 21005, USA

Correspondence
Department of Physics and Nuclear Engineering, United States Military Academy, West Point, NY, 10996, USA
Email: david.kashinski@westpoint.edu

Assessment of DFT methods through analysis of the Renner-Teller Effect (RTE) in the $X^2\Pi$ state of the NCO radical was completed. Our results suggest that the amount of exact exchange at long range is important for an accurate description of the RTE in NCO. DFT functionals from the B3LYP, PBE, TPSS, M06, and M11 families with standard Correlation Consistent, 6-311G split valence family, as well as Sadlej, and Sapporo polarized triple-ζ basis sets were assessed. Our Renner coefficients are compared with previously published theoretical and experimental results to characterize the overall accuracy of various functional/basis set combinations in determining the RTE splitting in the Π (bending) modes of NCO($X^2\Pi$). We suggest that this method of analysis can be extended to other systems, serve as an accuracy metric when selecting a functional, and provide a means to create training sets for machine learning in computational molecular physics applications.

KEYWORDS
Density Functional Theory (DFT), Renner-Teller Effect (RTE), Isocyanate Radical (NCO)

1 | INTRODUCTION

Density functional theory (DFT), in the common Kohn-Sham formalism [1], has become one of the go-to tools for the calculation of ground state observable properties of small and large molecular complexes. Its ease of use and its ability to produce accurate results at a cost less than traditional wavefunction methods has resulted in DFT being ubiquitously available in most (if not all) standard quantum chemistry packages.

In a recent study [2] employing DFT we realized that the out-of-box (OoB) calculation of harmonic vibrational modes using the GAUSSIAN09 [3] and now GAUSSIAN16 [4] suites render non-degenerate ground-state bending frequencies for open-shell linear molecules, specifically the NCO (isocyanate) radical. This lead us to question whether or not the software was predicting the Renner-Teller (RT) splitting of the bending modes to a useful level of accuracy and if so, what specifically makes one functional more or less accurate when determining the RT splitting.

Léonard *et al.* [5], and several references within, carried out a high-accuracy *ab initio* multi-reference configuration interaction with the Davidson correction (MRCI+Q) treatment of the Renner-Teller Effect (RTE) in NCO using the cc-pVTZ [6] basis set producing results with spectroscopic accuracy. Léonard *et al.*'s work shows the importance of electron correlation in systems such as NCO and due to this importance the authors suggest that DFT is not an appropriate method for treating the RTE in NCO to spectroscopic accuracy.

In this work we suggest that the amount of exact (or Hartree-Fock) electronic exchange correlation of a given functional strongly impacts the accuracy when treating the RTE in NCO. In order to establish this link we employ 13 common DFT functionals from the middle rungs of Perdew *et al.*'s metaphorical "Jacobs ladder" of functional accuracy [7], each with differing amounts of exact correlation, to determine the Renner coefficient from the non-degenerate bending vibrational modes of the NCO ground state ($X^2\Pi$). We then compare the results to experimental values and characterize the overall performance of these functionals classifying the impact of the electronic exchange energy on the accuracy of the results.

To our knowledge, the only other high-level DFT treatment of the RTE in NCO was completed by Mladenovic *et al.* [8] using only the B3LYP [9]/EPR-III [10] methods and no other work address the link between the amount of exact exchange energy and the accuracy of the DFT treatment of the RTE in NCO (or any other linear triatomics).

We also suggest that the OoB calculation of the RTE in NCO can serve as a metric to to assess the overall performance of a particular functional and basis set choice when using DFT for, or systems that include, bending NCO. We also speculate that this method can be extended to other open-shell linear triatomics. Understanding whether or not a functional will accurately predict the RT splitting in vibrational modes based on functional composition can be useful when working with open-shell linear molecules (like NCO) or systems with open-shell linear groups. We also suggest that this assessment method can also serve as a means for further developing training data sets for machine learning (ML) applications in molecular physics and quantum chemistry [11, 12].

2 | COMPUTATIONAL AND QUANTUM CHEMISTRY DETAILS

All calculations were completed using the GAUSSIAN16, Revision A.03, quantum chemistry suite [4]. Calculations utilized one or two compute nodes (two 16-core Intel Xeon E5-2698v3 [13] processors per node) housed in a Cray XC40 High Performance Computer (HPC) named "Excalibur". [1]

The DFT functionals used are a subset of those included in the standard GAUSSIAN16 suite [4, 14]. Namely, the TPSS [15, 16, 17], and M06 [18] families, as well as the M11 [19], B3LYP [9], CAM-B3LYP [20], B3PW91 [9, 21, 22,

---

[1] This HPC, formerly housed at the Army Research Laboratory, was decommissioned in February 2021; well after all calculations were complete.

23, 24], PBE [25, 26], and PBE0 [25, 26, 27] methods. We combine these functionals with the standard 6-311G series [28, 29, 30, 31, 32], correlation-consistent series [6, 33, 34, 35], and Sadlej polarized triple-ζ [36, 37, 38, 39, 40] basis sets, obtained through the Environmental Molecular Sciences Laboratory Basis Set Exchange [41, 42] (EMSL-BSE) database, as well as the Sapporo [43, 44, 45] polarized triple-ζ (SPK-TZP) and augmented-TZP (SPK-ATZP) basis sets along with the Sapporo 2012 updates [46, 45] (SPK-TZP-2012 and SPK-ATZP-2012). The basis sets employed in this study, except for the Sapporo sets obtained from Noro [46], were those tabulated on and downloaded from the EMSL-BSE [41, 42] database. Where possible, the basis sets obtained from the EMSL-BSE database were directly compared to those pre-programmed in GAUSSIAN16 to assure consistancy.

Each calculation used semi-default settings. We used keyword `Int(Grid = -96032)` to set a spherical numerical integration grid for all of our DFT calculations. The University of Minnesota Computational Chemistry website [47] and the GAUSSIAN reference website [48] outlines that this setting uses 96 radial shells around each atom with a spherical product grid of 32 θ and 64 ϕ points in each shell resulting in 196 608 integration points per atom. This keyword is often cited in benchmarking calculations [48] and effectively eliminates small imaginary (negative) frequencies [47].
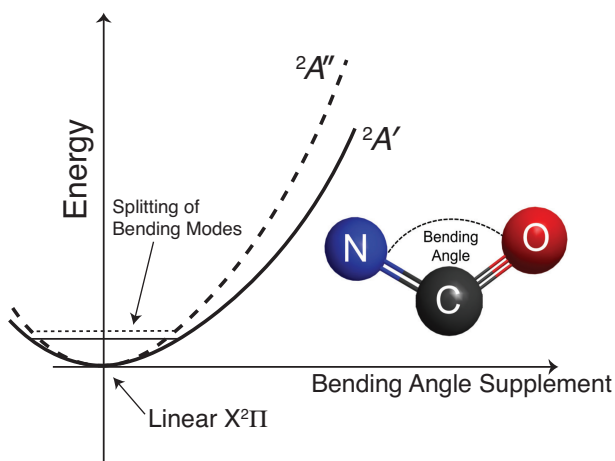
The unscaled harmonic vibrational frequencies for each functional/basis set combination were determined from the Hessian computed from the ground state stationary point. Calculations were completed in the typical C_{2v} point group (we note that linear NCO is in the $C_{\infty v}$ group) which was automatically selected by the GAUSSIAN16 software after reading the input file's z-matrix. Here we note that as part of the calculation process completed by GAUSSIAN16 the linear molecule is bent, therefore breaking the high-symmetry. The bent molecule is best described by the C_s point group which will be discussed more in section 3.

3 | THE RENNER-TELLER EFFECT AND THE NCO (ISOCYANATE) RADICAL

Gas phase NCO is of interest to us because of its presence in the residue of post-detonated chemical propellants [49, 50, 51, 2]. There is also a vast amount of information about NCO in the literature as this radical has been studied experimentally and theoretically since the late 1950's [52]. An extensive experimental treatment of the Renner-Teller levels in NCO was completed by Tan *et al.* [53] in 2003. Then, in 2004, R. Prasad [54] completed an exhaustive review of all the theoretical and experimental work on NCO and its isomers. We will not reproduce their results here except for instances where a specific result is relevant to the current work.

A linear triatomic molecule, ideally, has four irreducible vibrational modes (two non-degenerate and two degenerate) for a bound electronic state. In the $C_{\infty v}$ notation the non-degenerate Σ modes represent the symmetric and asymmetric stretching modes along the molecular axis (usually defined along the z-axis) and the degenerate Π modes represent the bending modes in the xy- and xz-plains. Open-shell linear triatomics (like NCO) have a non-zero projection of the electronic angular momentum onto the molecular axis that couples to the vibrational momenta. This coupling, known as the Renner-Teller (RT) coupling [55], results in a breakdown of the Born-Oppenheimer (BO) approximation [56] and the splitting of the ideally-degenerate bending (Π) modes [57] into two distinct observable values. The effect's namesake, Rudolf Renner, first described this splitting for linear CO_2 [58] in 1934. A good review of the original work is available online by Wormer [57] and an in-depth review of the RTE was done in 2019 by Jungen [59].

The breakdown of the BO approximation is manifest by a splitting of the two-fold degenerate potential energy surface (PES) representing the degenerate state. In the case of NCO, the linear ground state (in typical $C_{\infty v}$ notation) is $X^2\Pi$. As the molecule bends the high $C_{\infty v}$ symmetry is reduced to the less symmetric C_s point group with two irreducible symmetry representations: $^2A'$ and $^2A''$. The PESs representing the NCO($^2A'$) and NCO($^2A''$) states split as a function of the bending angle. We provide a sketch of this splitting in Fig. (1). NCO exhibits a "weak RTE" [60, 8, 61]

FIGURE 1 This figure presents a sketch of the "weak RTE" [60, 8, 61] in NCO. The origin represents ground state NCO in its linear configuration. The N-C and C-O bond lengths are kept at their respective equilibrium values. The horizontal axis is related to the molecular bending angle and the vertical is the typical potential energy. As the molecule bends the $^2A'$ (solid) and $^2A''$ (dashed) potential energy surfaces (PESs) split as a function of the bending angle. The vibrational spectra associated with each PES also split, represented by the horizontal solid and dashed lines near the bottom of the potential wells. The horizontal dashed line represents the higher-energy bending mode associated with the $^2A''$ PES (dashed) and the horizontal solid line represents the lower-energy bending mode associated with the $^2A'$ PES (solid). This is the Renner-Teller splitting of the bending modes in NCO($X^2\Pi$).

which is characterized by the small splitting between the non-degenerate $^2A'$ and $^2A''$ PESs each of which have their own vibrational spectra. For further reading on the weak RTE and a description of the the strong RTE see chapter 4 of Bersuker's book on the Jahn-Teller Effect [60].

3.1 | The Renner Coefficient (ε)

The Renner Coefficient (also known as the Renner Parameter), denoted ε, is a unit-less quantitative measure of the strength of the RTE (how much the ideally-degenerate bending (Π) mode splits). The RTE is characterized using the Renner coefficient [5],

$$\varepsilon = \frac{\omega_{A'}^2 - \omega_{A''}^2}{\omega_{A'}^2 + \omega_{A''}^2} \tag{1}$$

and by the average of the split frequencies,

$$\omega_{\text{avg}} = \frac{\omega_{A'}^2 + \omega_{A''}^2}{2} \tag{2}$$

where $\omega_{A'}^2$ and $\omega_{A''}^2$ represent the bending frequencies in units of cm^{-1} in the harmonic approximation. For $\varepsilon < 0$ the bending mode associated with the $^2A'$ PES is lower in energy than the mode associated with the $^2A''$ PES. This is the situation is sketched in Fig. (1). For all of our calculated results $\varepsilon < 0$. In Table (1) we provide relevant values for ω_{avg} and ε found in the literature. In Table (2), in this articles appendix, we provide all of our calculated Renner coefficents.

Due to the same dimensionality of the numerator and denominator in Eq. (1) the method-dependent global mul-

TABLE 1　Relevant Renner Coefficients (ε), also called the Renner Parameter, found in the literature for NCO($X^2\Pi$). The ω_{avg} parameter is the typical arithmetic mean of the respective $^2A'$ and $^2A''$ bending modes in units of wavenumbers (cm^{-1}). In the present work we compare our values to $\varepsilon = (-0.1436 \pm 0.0001)$ [62, 63]. The value for the absolute uncertainty was determined to be 0.000057 using values presented in Prasad's review [54] and the method of quadrature outlined by Taylor [64] and rounded to a more conservative 0.0001. We provide other values for context on the uncertainty that may exist in the value.

Type	ω_{avg}	ε
Theoretically Determined Values		
B3LYP/EPR-III, Mladenovic *et al.* [8]	540	-0.15
MRCI+Q/cc-pVQZ, Léonard *et al.* [5]	532	-0.1441
fv-CASSCF [a]/6s4p2d2f, Prasad [54]	532	-0.124
CAM-B3LYP/aug-cc-pCvQZ [Fig. (2)], this work	543.74[b]	-0.1424
M06/cc-pVDZ, this work	537.38[c]	-0.14365
Experimentally Determined Values		
Tables 5 & 6, Wu *et al.* [62]	532.69	-0.1436
Table 4, Woodward *et al.* [63]	528.6	-0.1436
NIST [65]	535.4	-
Tables 2 & 3, Dixon [52]	539.4	-0.181

[a]full-valence Complete Active Space Self-Consistent-Field (fv-CASSCF).
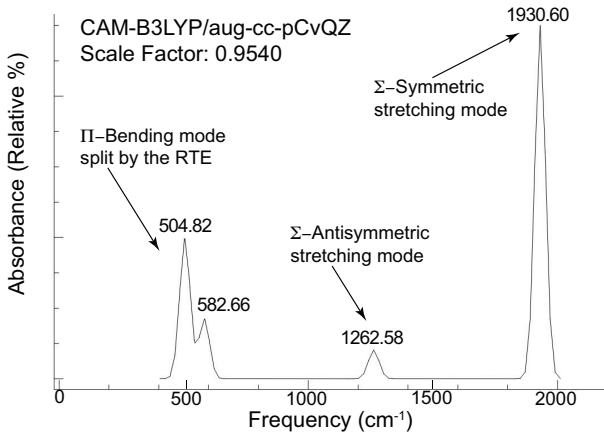[b]Calculated frequencies are scaled by 0.9540 [2].
[c]Calculated frequencies are scaled by 0.9620 [2].

tiplicative linear harmonic scaling factors, used to account for anharmonicity when the harmonic approximation is employed [66, 67, 68, 2], reduces to unity so we need not scale our harmonic frequencies before computing the Renner coefficient. The ω_{avg}, however, does require scaling of the harmonic frequencies when comparing to experimental counterparts. Appropriate scaling factors can be found in the literature (for example see Ref. [2] and references within) and some are provided by NIST. Except for the frequencies presented in Fig. (2) and the ω_{avg}'s in Table (1) we did not apply scaling factors in this study.

The splitting of the vibrational bending modes due to the RTE in NCO was observed experimentally in 1960 by Dixon [52]. In Fig. (2) we provide a simulation [69] of the NCO($X^2\Pi$) vibrational absorption spectra. The bending mode split by the RTE is indicated in the figure as are the symmetric and antisymmetric stretching modes. The frequencies in the simulation are calculated at the CAM-B3LYP/aug-cc-pCvQZ level and scaling factor of 0.9540 [2] was applied. CAM-B3LYP is a Range Separated Hybrid (RSH) functional with a mid-to-long range exact correlation contribution of 65%. This will be discussed more in section 4.1. The Renner coefficient and ω_{avg} for this calculation are given in Table (1) for direct comparison with the literature. The calculated frequencies are in very good agreement with the experimental values of 535.4 cm^{-1}, 1266.6 cm^{-1}, and 1921.3 cm^{-1} reported on the NIST [65] database.

4 | CHARACTERIZATION AND DISCUSSION

The motivation behind this preliminary study was to use the RT splitting of the bending modes in the ground state of the NCO radical as a metric to assess and characterize the performance of various functional and basis set choices in order to establish a link between the accuracy of the calculated Renner coefficient and the amount of exact correlation in a given functional. In all we completed 273 calculations (13 functionals 21 basis sets). However, because of weak across-the-board performance of the 6-311G basis set (which was expected), we excluded those 13 calculations from the remainder of our analysis.

FIGURE 2 This figure presents a simulation [69] of the vibrational absorption spectra for the NCO($X^2\Pi$) radical. The vertical axis is relative absorbance scaled against the absolute absorbance of the symmetric stretching mode (set to 100%). The frequencies are calculated at the CAM-B3LYP/aug-cc-pCvQZ level and scaling factor of 0.9540 [2] was applied. The calculated frequencies are in very good agreement with the experimental values reported on the NIST [65] database. The resulting Renner-coefficient, $\varepsilon = -0.1424$, is in excellent agreement with the experimentally determined -0.1436 [62, 63].

We compute the mean absolute relative error (MARE) from the experimentally determined "target" Renner coefficient in usual way; illustrated by:
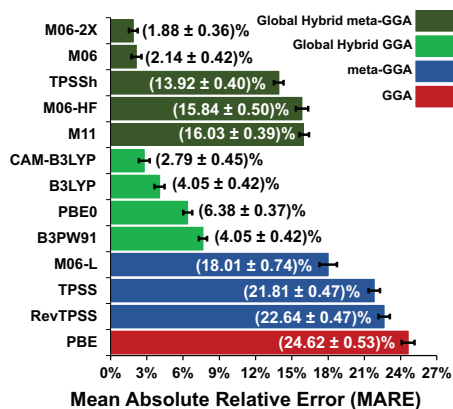
$$\text{MARE} = \frac{1}{n} \sum_{i=1}^{n} \left| \frac{\varepsilon_i - \varepsilon_{\text{target}}}{|\varepsilon_{\text{target}}|} \right| \tag{3}$$

where ε_i represents the presently calculated Renner coefficient, $\varepsilon_{\text{target}} = -0.1436$ represents the experimentally determined Renner coefficient [5, 63], and n is the total number of coefficients sampled per functional (20 in this case). The fraction inside of the absolute value bars of the summation is the relative error (RE) of a particular method combination (also called relative difference (RD) in the literature). The MARE is used to characterize our results. In Fig. (3) we graphically present the MAREs as well as the actual MARE value for each functional with an error bar representing the standard error (SE) for the functional in question assessed across the $n = 20$ basis sets. For each functional we compute the SE using

$$\text{SE} = \frac{\sigma}{\sqrt{n}} \tag{4}$$

where σ represents the standard deviation across the sampled basis sets. The relative error (RE) of the calculated coefficients, when compared to the target value, approximate a normal distribution about the average value, as illustrated in Fig. (4).

The base 6-311G basis set showed weak performance across all functionals which was expected. The weakest was M06-HF/6-311G yielding $\varepsilon = -0.0368$, a $+74.4\%$ relative error (RE) from our target value. On average, the 6-311G basis set results in a $(26.6 \pm 6.9)\%$ MARE when assessed across all 13 functionals. The 6.9% error bar is computed using the SE described in Eq. (4) assessed across the 13 functionals. The next weakest performance was the PBE/aug-cc-pVDZ which yielded $\varepsilon = -0.1871$, a -30.3% RE from our target value. Overall, the PBE functional showed a weak

FIGURE 3 This figure presents the MAREs, as defined by Eq. (3), for each functional assessed. The error bar represents the standard error (SE) as determined using Eq. (4) as assessed over the 20 basis sets sampled. The color code ties the functionals to their rung of Perdew *et al.*'s metaphorical "Jacob's Ladder" of functional approximation accuracy [7, 70]. In this figure we separate "rung four" into two shades of green highlighting the differences between Hybrid GGA (light green) and Hybrid meta-GGA (dark green) functionals. Functionals from the lowest rung, Local Spin-Density Approximation (LSDA), were not assessed in this study.

performance across all 20 basis sets yielding a $(-24.62 \pm 0.53)\%$ MARE from the target value.
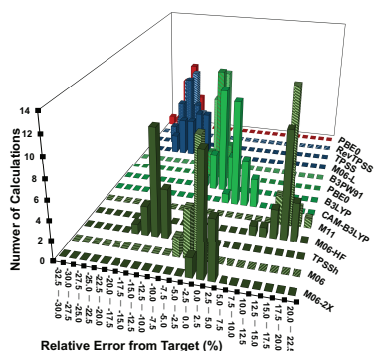
The overall strongest performance was M06/cc-pVDZ yielding $\varepsilon = -0.14365$, a -0.033% RE from our target value. This result is interesting because in general the aug-cc-pVDZ basis set shows a weaker across-the-board performance with a $(15.0\pm3.9)\%$ MARE when assessed across all 13 functionals. Overall M06 performed well yielding a $(2.14\pm0.42)\%$ MARE. But, the M06-2X functional performed best resulting in a $(1.88 \pm 0.36)\%$ MARE.

In Fig. (3) we present the MARE values for the functional families assessed. The color code indicates where the functionals lie on Perdew *et al.*'s metaphorical "Jacob's Ladder" of functional approximation accuracy [7, 70]. As one would expect, the global hybrid GGA and global hybrid meta-GGA perform better than than the meta-GGA and pure GGA functionals. The small SE, indicated by the error bars, supports the suggestion that results determined with DFT have a stronger dependence on functional choice than on the choice of basis set [2, 71].

In Fig. (5) we present the average Renner coefficient determined for each functional assessed depicting where it lies on a number line compared to the target value. Although very small, we do include an error bar computed using the SE of the 20 basis sets assessed. All of our calculated Renner coefficients are provided in Table (2) and the resulting REs from the target value as well as the MAREs are provided in Table (3) of this article's appendix.

4.1 | Linking Exact Exchange Energy to the Accuracy of ε

Accurate treatment of the electronic correlation has proven to be very important when calculating the Renner coefficient to spectroscopic accuracy [5]. Analysis of the MAREs of the Hybrid GGA and Hybrid meta-GGA functionals in Fig. (3) suggests that accuracy of a calculated Renner coefficient is dependent on the amount of exact exchange energy (also called Hartree-Fock exchange energy and is often denoted E_x^{HF} in the literature [72, 70]) that is included in the functional's total exchange-correlation energy term (typically denoted E_{xc} in the literature [72, 70]). M06 and M06-2X have 27% and 54% HF exchange respectively [18] with the M06-2X performing marginally better than M06. However, the M06-HF [18] with its 100% HF exchange performs significantly worse. The range separated hybrid (RSH) M11 functional [19], with its 42.8% short range and 100% long rage HF exchange, performs about the same
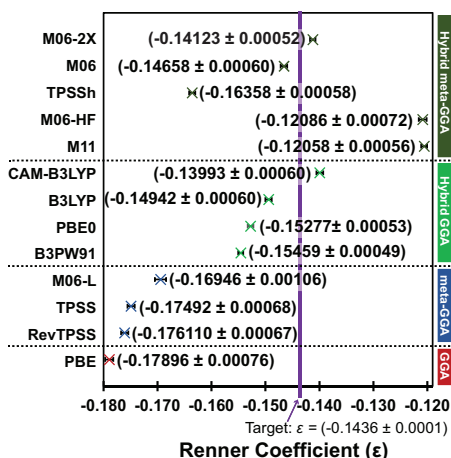
FIGURE 4 This figure presents the relative error (RE) from the target, as defined by the fraction in Eq. (3), for each coefficient for each functional assessed across all basis sets sampled. This figure is intended to be qualitative in nature showing that for each functional, the REs from the target approximate a normal distribution about the average RE. The the horizontal bins are 2.5% RE from the target. The color code is similar to that used in Fig (3) used to distinguish the placement on Jacob's ladder. In areas where distributions overlap we add a pattern to allow distinguishable results. Due to is across-the-board poor performance the 13 coefficients resulting from the 6-311G basis set are not included in this analysis. The remaining 260 coefficients tabulated and shown.

as M06-HF suggesting that this system has a stronger longer-range dependence on the exact exchange contribution. The improved performance of CAM-B3LYP over B3LYP supports this suggestion. At short range CAM-B3LYP [20] has 19% while at mid-to-long range it has a 65% exact exchange while B3LYP [9] maintains a constant 20% exact exchange at all ranges. The M06, M06-2X, and CAM-B3LYP showed great performance when compared to the other functionals assessed. This preliminary assessment suggests that the accuracy of the calculated Renner coefficient has definite dependence on the amount of exact exchange energy contribution at mid-to-long range and that this contribution lies between ∼30% (M06-2x) and ∼70% (CAM-B3LYP) (when rounded to one significant figure).

5 | SUMMARY & CONCLUDING REMARKS

The GAUSSIAN16 quantum chemistry suite on DoD-HPCMP HPCs was used to compute the ground state ($X^2\Pi$) vibrational modes of the NCO radical using Density Functional theory (DFT). The out-of-box bending (Π) vibrational modes calculated by the software shows the splitting in the ideally degenerate bending modes associated with the NCO($X^2\Pi$) state due to the Renner-Teller effect (RTE). We used these non-degenerate bending modes to calculate the Renner coefficient (ε) for 21 common basis sets assessed across 13 common functionals residing on various rungs of Jacob's ladder. For each functional assessed we computed the mean absolute relative error (MARE) from the experimentally determined "target" value for the NCO($X^2\Pi$) Renner coefficient found in the literature. As expected, we found a weak across-the-board performance of the 6-311G basis set so these 13 data points were excluded from the overall analysis. Upon analyzing results across the reaming 20 basis sets, we find that the M06-2X, M06, and CAM-B3LYP functionals perform the best with respect to the other 10 functionals assessed. Results of this preliminary study suggest that the accuracy of the DFT-calculated Renner coefficient is highly dependent on the longer-range contribution of the exact (or Hartree-Fock) exchange energy (E_x^{HF}) in the functional's exchange-correlation energy term (E_{xc}). We are suggesting that use of DFT to calculate the effects of the RTE in open shell linear molecules may serve as a metric for assessing the likelihood of accurate performance when calculating vibronic effects in similar

FIGURE 5 This figure presents the average Renner coefficients for the indicated functional on a number line as it compares to the experimentally determined "target" value indicated by the vertical purple line. The error bar represents the standard error (SE) determined using Eq. (4) as assessed over the 20 basis sets sampled. The color code used is the same as that used in Fig. (3).

species or larger systems with isocyanate groups *a priori*. This method may also be applicable for inclusion in much needed machine learning training sets [11, 12] for molecular physics and quantum chemistry applications where near-spectroscopic accuracy is desired.

Research Resources

conflict of interest

The views expressed herein are those of the authors and do not purport to reflect the position of the United States Military Academy, Army Research Laboratory, US Department of the Army, or US Department of Defense.

references

[1] Kohn W, Sham LJ. Self-Consistent Equations Including Exchange and Correlation Effects. Phys Rev 1965;140:A1133–A1138.

[2] Kashinski DO, Chase GM, Nelson RG, Nallo OED, Scales AN, VanderLey DL, et al. Harmonic Vibrational Frequencies:

Approximate Global Harmonic Scaling Factors for TPSS, M06, and M11 Functional Families using Several Common Basis Sets. J Phys Chem A 2017;121:2265−-2273.

[3] Frisch MJ, Trucks GW, Schlegel HB, Scuseria GE, Robb MA, Cheeseman JR, et al., Gaussian 09 Revision E.01;. Gaussian Inc. Wallingford CT 2009.

[4] Frisch MJ, Trucks GW, Schlegel HB, Scuseria GE, Robb MA, Cheeseman JR, et al., Gaussian 16 Revision C.01; 2016. Gaussian Inc. Wallingford CT 2016.

[5] Léonard C, Gritli H, Chambaud G. Ab initio study of the spectroscopy of the $X^2\Pi$ electronic ground states of CNO and NCO. J Mol Spec 2007;243:90–98.

[6] Dunning TH. Gaussian basis sets for use in correlated molecular calculations. I. The atoms boron through neon and hydrogen. J Chem Phys 1989;90:1007–1023.

[7] Perdew JP, Ruzsinszky A, Tao T. Prescription for the design and selection of density functional approximations: More constraint satisfaction with fewer fits. J Chem Phys 2005;123:062201.

[8] Mladenović M, Miljenko P, Bernd E. An ab initio study of the vibronic, spin-orbit, and magnetic hyperfine structure in the $X^2\Pi$ electronic state of NCO. J Chem Phys 2005;122:144306.

[9] Becke AD. Density-functional thermochemistry. III. The role of exact exchange. J Phys Chem 1993;98:5648–5652.

[10] Barone V. Recent Advances in Density Functional Methods, Part I. World Scientific Publ. Co.; 1996.

[11] Dral PO. Quantum Chemistry in the Age of Machine Learning. J Phys Chem Lett 2020;11:2336–2347.

[12] Rupp M. Machine Learning for Quantum Mechanics in a Nutshell. International Journal of Quantum Chemistry 2015;115:1058–1073.

[13] Intel Xeon Processor E5-2698 v3, WWW Page; 2016. `http://ark.intel.com/products/81060/Intel-Xeon-Processor-E5-2698-v3-40M-Cache-2\_30-GHz`.

[14] Gaussian09 Users Reference; Density Functional (DFT) Methods, WWW Page;, accessed: August, 2013.

[15] Tao JM, Perdew JP, Staroverov VN, Scuseria GE. Climbing the density functional ladder: Nonempirical meta-generalized gradient approximation designed for molecules and solids. Phys Rev Lett 2003;91:146401.

[16] Perdew JP, Ruzsinszky A, Csonka GI, Constantin LA, J S. Workhorse Semilocal Density Functional for Condensed Matter Physics and Quantum Chemistry. Phys Rev Lett 2009;103:026403.

[17] Perdew JP, Ruzsinszky A, Csonka GI, Constantin LA, J S. Erratum: 'Workhorse Semilocal Density Functional for Condensed Matter Physics and Quantum Chemistry. Phys Rev Lett 2011;106:179902(E).

[18] Zhao Y, Truhlar DG. The M06 suite of density functionals for main group thermochemistry, thermochemical kinetics, noncovalent interactions, excited states, and transition elements: two new functionals and systematic testing of four M06-class functionals and 12 other functionals. Theor Chem Acc 2008;120:215–241.

[19] Peverati R, Truhlar DG. Improving the Accuracy of Hybrid Meta-GGA Density Functionals by Range Separation. J Phys Chem Lett 2011;2:2810–2817.

[20] Yanai T, Tew D, Handy N. A new hybrid exchange-correlation functional using the Coulomb-attenuating method (CAM-B3LYP). Chem Phys Lett 2004;393:51–57.

[21] Perdew JP, Chevary JA, Vosko SH, Jackson KA, Pederson MR, Singh DJ, et al. Atoms, molecules, solids, and surfaces: Applications of the generalized gradient approximation for exchange and correlation. Phys Rev B 1992;46:6671–6687.

[22] Perdew JP, Chevary JA, Vosko SH, Jackson KA, Pederson MR, Singh DJ, et al. Erratum: Atoms, molecules, solids, and surfaces - Applications of the generalized gradient approximation for exchange and correlation. Phys Rev B 1993;48:4798.

[23] Perdew JP, Burke K, Wang Y. Generalized gradient approximation for the exchange-correlation hole of a many-electron system. Phys Rev B 1996;54:16533–16539.

[24] Burke K, Perdew JP, Wang Y. Electronic Density Functional Theory: Recent Progress and New Directions. J Phys Chem 1993;98:5648–5652.

[25] Perdew JP, Burke K, Ernzerhof M. Generalized gradient approximation made simple. Phys Rev Lett 1996;77:3865–3868.

[26] Perdew JP, Burke K, Ernzerhof M. Errata: Generalized gradient approximation made simple. Phys Rev Lett 1997;78:1396.

[27] Adamo C, Barone V. Toward reliable density functional methods without adjustable parameters: The PBE0 model. J Chem Phys 1999;110:6158–6169.

[28] McLean AD, Chandler GS. Contracted Gaussian-basis sets for molecular calculations 1. 2nd row atoms, Z = 11–18. J Chem Phys 1980;72:5639–5648.

[29] Raghavachari K, Binkley JS, Seeger R, Pople JA. Self-Consistent Molecular Orbital Methods. 20. Basis set for correlated wave-functions. J Chem Phys 1980;72:650–654.

[30] Hariharan PC, Pople JA. Theoret Chimica Acta 1973;28:213.

[31] Francl MM, Petro WJ, Hehre WJ, Binkley JS, Gordon MS, DeFrees DJ, et al. J Chem Phys 1982;77:3654.

[32] Clark T, Chandrasekhar J, Spitznagel GW, Schleyer PVR. J Comp Chem 1983;4:294.

[33] Kendall RA, Jr THD, Harrison RJ. Electron affinities of the first-row atoms revisited. Systematic basis sets and wave functions. J Chem Phys 1992;96:6796–806.

[34] Davidson ER. Comment on 'Comment on Dunning's correlation-consistent basis sets'. Chem Phys Lett 1996;260:514–518.

[35] Woon DE, T H Dunning J. J Chem Phys 1995;103:4572.

[36] Sadlej AJ. Collec Czech Chem Commun 1988;53:1995.

[37] Sadlej AJ, Urban M. J Mol Struct (THEOCHEM) 1991;234:147.

[38] Sadlej AJ. Theor Chim Acta 1992;79:123.

[39] Sadlej AJ. Theor Chim Acta 1992;81:45.

[40] Sadlej AJ. Theor Chim Acta 1992;81:339.

[41] Feller D. The Role of Databases in Support of Computational Chemistry Calculations. J Comp Chem 1996;17(13):1571–1586.

[42] Schuchardt KL, Didier BT, Elsethagen T, Sun L, Gurumoorthi V, Chase J, et al. Basis Set Exchange: A Community Database for Computational Sciences. J Chem Inf Model 2007;47(3):1045–1052.

[43] Noro T, Sekiya M, Koga T. Contracted polarization functions for the atoms helium through neon. Theoret Chem Acc 1997;98:25–32.

[44] Noro T, Sekiya M, Koga T. Correlating basis sets for the H atom and the alkali-metal atoms from Li to Rb. Theoret Chem Acc 2003;109:85–90.

[45] Segmented Gaussian Basis Set, Quantum Chemistry Group, Sapporo, Japan; 2014, `http://sapporo.center.ims.ac.jp/sapporo/`.

[46] Noro T, Sekiya M, Koga T. Segmented contracted basis sets for atoms H through Xe: Sapporo-(DK)-nZP sets (n = D, T, Q). Theoret Chem Acc 2012;131:1124.

[47] Minnesota density functionals available in Gaussian09, WWW Page; February, 2016, `http://comp.chem.umn.edu/info/G09.html`.

[48] Gaussian09 Users Reference; Integral;. Accessed: May, 2013. http://www.gaussian.com/g_tech/g_ur/k_integral.htm.

[49] Rocchio JJ, May IW. Analysis of Exhaust Gasses From the XM-19 Rifle – An application og Gas Chromatography/Mass Spectroscopy. Aberdeen Proving Ground, MD: Ballistic Research Laboratories; 1973.

[50] ; Spring 2013. Weapons and Materials Research Directorate, Army Research Laboratory, Aberdeen, MD, Private Communication.

[51] Haynes BS. The oxidation of hydrogen cyanide in fuel-rich flames. Combustion and Flame 1977;28:113–121.

[52] Dixon RN. The absorption spectrum of the free NCO radical. Philosophical Transactions of the Royal Society A 1960;252:165.

[53] Tan X, Dagdigian PJ. Vibrational energy transfer involving Renner-Teller levels of the NCO($X^2\Pi$) molecule. Chem Phys Lett 2003;375:532–539.

[54] Prasad R. A theoretical study of the fine and hyperfine interactions in the NCO and CNO radicals. J Chem Phys 2004;120:10089–10099.

[55] Herzberg G, Teller E. Schwingungsstruktur der Elektronenübergänge bei mehratomigen Molekülen. Zeitschrift für Physikalische Chemie 1933;21B:410–446.

[56] Hanson DM, Harvey E, Sweeney R, Zielinski TJ, The Born-Oppenheimer Approximation. Chemical Education Digital Library (ChemEd DL); 2020. `https://chem.libretexts.org/@go/page/1973`, [Online; accessed 2021-03-23].

[57] The original Renner-Teller effect, WWW PDF; 2003, `https://www.theochem.ru.nl/files/dbase/renner-teller-wormer-1dec2003.pdf`.

[58] Renner R. Zur Theorie der Wechselwirkung zwischen Elektronen- und Kernbewegung bei dreiatomigen, stabförmigen Molekülen. Zeitschrift für Physik volume 1934;92:172–193.

[59] Jungen C. The Renner-Teller effect revisited 40 years later. J Mol Spec 2019;363:111172.

[60] Bersuker I. In: Pseudo Jahn–Teller, product Jahn–Teller, and Renner–Teller effects Cambridge University Press; 2006. p. 110–161.

[61] Perić M, Hess BA, Buenker RJ. Ab inito MRD-CI study of the Renner-Teller effect and spin-orbit coupling in the $X^2\Pi$ ground state of NCO. Mol Phys 1986;58:1001–1011.

[62] Wu M, Northrup FJ, Sears TJ. Study of Renner-Teller, spin-orbit, and Fermi-resonance interactions in $X^2\Pi(v_1\, v_2\, 0)$ levels of NCO by stimulated emission pumping spectroscopy. J Chem Phys 1992;97:4583.

[63] Woodward DR, Fletcher DA, Brown JM. Dispersed fluorescence studies of the NCO radical Fermi resonance between the (100) and (020) levels of the $X^2\Pi$ state. Mol Phys 1987;62:517–536.

[64] Taylor JR. An Introduction to Error Analysis The Study of Uncertainties in Physical Measurements. 2 ed. University Science Books; 1997.

[65] NIST Computational Chemistry Comparison and Benchmark Database, WWW Page; 2013, `http://cccbdb.nist.gov`.

[66] Pople JA, Schlegel HB, Krishnan R, Defrees DJ, Binkley JS, Frisch MJ, et al. Molecular orbital studies of vibrational frequencies. Int J Quantum Chem, Quantum Chem Symp 1981;15:269–278.

[67] Scott AP, Radom L. Harmonic Vibrational Frequencies: An Evaluation of Hartree-Fock, Mø"ller-Plesset, Quadratic Configuration Interaction, Density Functional Theory, and Semiempirical Scale Factors. J Phys Chem 1996;100:16502–16513.

[68] Sinha P, E BS, Gu C, Wheeler RA, Wilson AK. Harmonic Vibrational Frequencies: Scaling Factors for HF, B3LYP, and MP2 Methods in Combination with Correlation Consistent Basis Sets. J Phys Chem A 2004;108:9213–9217.

[69] Avogadro: advanced molecule editor and visualizer, WWW Page; 2021. `https://avogadro.cc`.

[70] Mardirossian N, Head-Gordon M. Thirty years of density functional theory in computational chemistry: an overview and extensive assessment of 200 density functionals. Molecular Physics 2017;115:2315–2372.

[71] Friese DH, Törk L, Hättig C. Vibrational frequency scaling factors for correlation consistent basis sets and the methods CC2 and MP2 and their spin-scaled SCS and SOS variants. J Chem Phys 2014;141:194106.

[72] Burke K, Wagner LO. DFT in a Nutshell. International Journal of Quantum Chemistry 2013;113:96–101.

Appendix: Calculated Values

In this appendix we include the calculated Renner coefficients (ε) in Table (2) and the percent relative error (%-RE) of the calculated ε from the experimentally determined "target" value in Table (3).

TABLE 2 All of the Renner Coefficients we calculated using Eq. (1). The arithmetic mean and standard deviation of the mean (σ) are computed in the usual way. The standard error (SE) for each functional is computed using Eq. (4). The left to right order of the functionals is that of the top-down order in Fig. (3). The functional column labeled CB3LYP is shorthand for CAM-B3LYP.

Basis/Func	M06-2X	M06	TPSSh	M06-HF	M11	CB3LYP	B3LYP	PBE0	B3PW91	M06-L	TPSS	RevTPSS	PBE
aug-cc-pVTZ	-0.14176	-0.14499	-0.16300	-0.12324	-0.12173	-0.14088	-0.14981	-0.15270	-0.15430	-0.16615	-0.17403	-0.17511	-0.17847
aug-cc-CpVTZ	-0.14162	-0.14449	-0.16283	-0.11899	-0.12082	-0.14064	-0.14954	-0.15249	-0.15408	-0.16476	-0.17384	-0.17493	-0.17809
aug-cc-pVQZ	-0.14376	-0.15026	-0.16498	-0.11969	-0.12074	-0.14234	-0.15144	-0.15444	-0.15613	-0.17202	-0.17611	-0.17756	-0.18028
aug-cc-CpVQZ	-0.14346	-0.15039	-0.16474	-0.11951	-0.11912	-0.14242	-0.15151	-0.15442	-0.15612	-0.17333	-0.17584	-0.17732	-0.18044
aug-cc-pVDZ	-0.14674	-0.15229	-0.16996	-0.12541	-0.12534	-0.14695	-0.15660	-0.15908	-0.16060	-0.17797	-0.18199	-0.18302	-0.18705
cc-pVTZ	-0.14123	-0.14522	-0.16318	-0.12587	-0.12352	-0.13913	-0.14837	-0.15172	-0.15399	-0.16642	-0.17439	-0.17526	-0.17706
cc-CpVTZ	-0.13951	-0.14368	-0.16128	-0.12069	-0.12075	-0.13727	-0.14635	-0.15002	-0.15221	-0.16444	-0.17218	-0.17314	-0.17461
cc-pVQZ	-0.14334	-0.15106	-0.16398	-0.12393	-0.12354	-0.14144	-0.15056	-0.15370	-0.15567	-0.17212	-0.17494	-0.17669	-0.17919
cc-pVDZ	-0.13833	-0.14365	-0.16463	-0.11568	-0.11285	-0.13539	-0.14661	-0.15262	-0.15403	-0.17412	-0.17706	-0.17773	-0.18071
6-311G(p)	-0.13980	-0.14760	-0.16579	-0.11797	-0.11819	-0.13783	-0.14882	-0.15365	-0.15554	-0.17521	-0.17818	-0.17915	-0.18180
G(pd)	-0.13980	-0.14760	-0.16579	-0.11797	-0.11819	-0.13783	-0.14882	-0.15365	-0.15554	-0.17521	-0.17818	-0.17915	-0.18180
++G(pd)	-0.14301	-0.14823	-0.16749	-0.11982	-0.12009	-0.14185	-0.15245	-0.15603	-0.15746	-0.17652	-0.17963	-0.18112	-0.18405
++G(2p2d)	-0.14158	-0.14516	-0.16155	-0.12195	-0.12141	-0.14074	-0.14918	-0.15165	-0.15313	-0.16965	-0.17231	-0.17410	-0.17649
++G(2df2dp)	-0.14002	-0.14263	-0.15998	-0.11978	-0.12123	-0.13918	-0.14769	-0.15003	-0.15176	-0.16386	-0.17074	-0.17203	-0.17512
++G(3df3dp)	-0.14165	-0.14497	-0.16347	-0.12100	-0.12122	-0.14156	-0.15059	-0.15323	-0.15481	-0.16537	-0.17456	-0.17585	-0.17917
Sadlej	-0.14262	-0.14704	-0.16434	-0.12928	-0.12193	-0.14162	-0.15123	-0.15323	-0.15541	-0.17053	-0.17607	-0.17682	-0.18121
SPK-TZP	-0.13757	-0.14526	-0.16025	-0.11978	-0.12050	-0.13577	-0.14557	-0.14934	-0.15190	-0.16626	-0.17126	-0.17227	-0.17447
SPK-ATZP	-0.14124	-0.14639	-0.16270	-0.11962	-0.12090	-0.14072	-0.14965	-0.15256	-0.15420	-0.16578	-0.17361	-0.17486	-0.17803
SPK-TZP-2012	-0.13663	-0.14443	-0.15925	-0.11865	-0.11978	-0.13447	-0.14427	-0.14835	-0.15092	-0.16461	-0.17017	-0.17129	-0.17328
SPK-ATZP-2012	-0.14094	-0.14621	-0.16249	-0.11831	-0.11978	-0.14050	-0.14939	-0.15240	-0.15401	-0.16489	-0.17335	-0.17467	-0.17787
Mean:	-0.14123	-0.14658	-0.16358	-0.12086	-0.12058	-0.13993	-0.14942	-0.15277	-0.15459	-0.16946	-0.17492	-0.17610	-0.17896
σ:	0.00234	0.00270	0.00258	0.00324	0.00251	0.00291	0.00270	0.00238	0.00219	0.00472	0.00304	0.00302	0.00339
SE :	0.00052	0.00060	0.00058	0.00072	0.00056	0.00065	0.00060	0.00053	0.00049	0.00106	0.00068	0.00067	0.00076

TABLE 3   Relative error (RE) of the calculated Renner Coefficients from the experimentally determined target value of $\varepsilon = -0.1436$ [5, 63]. The values below are percents (%). At the bottom of the table, for each functional, we compute the Mean Absolute Relative Error (MARE) using Eq. (3). The individual REs are determined using the fractional argument of of the summation in Eq. (3). The standard deviation of the mean (σ) is computed in the usual way from which the standard error (SE) is computed using Eq. (4). The left to right order of the functionals is that of the top-down order in Fig. (3). The functional column labeled CB3LYP is shorthand for CAM-B3LYP.

Basis/Func	M06-2X	M06	TPSSh	M06-HF	M11	CB3LYP	B3LYP	PBE0	B3PW91	M06-L	TPSS	RevTPSS	PBE	MARE	σ	SE
aug-cc-pVTZ	1.282	-0.968	-13.508	14.178	15.231	1.897	-4.325	-6.337	-7.448	-15.705	-21.191	-21.946	-24.283	11.41	12.81	3.56
aug-cc-CpVTZ	1.381	-0.618	-13.389	17.140	15.860	2.062	-4.133	-6.190	-7.297	-14.735	-21.057	-21.817	-24.015	11.52	12.23	3.67
aug-cc-pVQZ	-0.114	-4.639	-14.891	16.652	15.917	0.875	-5.457	-7.552	-8.727	-19.788	-22.636	-23.652	-25.543	12.80	13.82	3.83
aug-cc-CpVQZ	0.098	-4.731	-14.719	16.779	17.046	0.821	-5.507	-7.534	-8.717	-20.706	-22.451	-23.480	-25.651	12.94	14.04	3.90
aug-cc-pVDZ	-2.189	-6.054	-18.357	12.670	12.714	-2.332	-9.051	-10.780	-11.839	-23.937	-26.736	-27.453	-30.256	14.95	14.19	3.94
cc-pVTZ	1.651	-1.127	-13.634	12.349	13.987	3.115	-3.322	-5.656	-7.239	-15.895	-21.440	-22.045	-23.301	11.14	12.45	3.45
cc-CpVTZ	2.848	-0.057	-12.309	15.952	15.911	4.406	-1.918	-4.469	-5.994	-14.515	-19.902	-20.574	-21.595	10.80	12.73	3.53
cc-pVQZ	0.180	-5.194	-14.194	13.697	13.969	1.503	-4.846	-7.031	-8.409	-19.857	-21.821	-23.041	-24.783	12.19	12.93	3.59
cc-pVDZ	3.669	-0.033	-14.646	19.446	21.416	5.716	-2.095	-6.281	-7.263	-21.250	-23.300	-23.767	-25.844	13.44	15.80	4.38
6-311G(p)	2.648	-2.788	-15.450	17.851	17.698	4.019	-3.634	-7.002	-8.315	-22.012	-24.080	-24.759	-26.604	13.61	15.17	4.21
G(pd)	2.648	-2.788	-15.450	17.851	17.698	4.019	-3.634	-7.002	-8.315	-22.012	-24.080	-24.759	-26.604	13.61	15.17	4.21
++G(pd)	0.408	-3.225	-16.637	16.562	16.369	1.220	-6.163	-8.653	-9.652	-22.924	-25.091	-26.130	-28.165	13.94	15.01	4.16
++G(2p2d)	1.405	-1.089	-12.498	15.074	15.455	1.989	-3.884	-5.604	-6.633	-18.140	-19.996	-21.237	-22.907	11.22	12.77	3.54
++G(2df2dp)	2.490	0.674	-11.410	16.589	15.580	3.079	-2.847	-4.481	-5.681	-14.108	-18.899	-19.798	-21.947	10.58	12.49	3.46
++G(3df3dp)	1.359	-0.956	-13.834	15.741	15.586	1.419	-4.869	-6.704	-7.803	-15.158	-21.560	-22.457	-24.770	11.71	13.19	3.66
Sadlej	0.680	-2.398	-14.440	9.970	15.092	1.376	-5.310	-6.704	-8.226	-18.757	-22.612	-23.134	-26.188	11.91	12.88	3.57
SPK-TZP	4.199	-1.157	-11.594	16.584	16.086	5.451	-1.369	-3.998	-5.778	-15.783	-19.264	-19.962	-21.495	10.99	12.88	3.57
SPK-ATZP	1.643	-1.945	-13.298	16.698	15.805	2.008	-4.211	-6.238	-7.382	-15.443	-20.896	-21.766	-23.973	11.64	13.14	3.64
SPK-TZP-2012	4.854	-0.576	-10.899	17.374	16.584	6.355	-0.469	-3.307	-5.099	-14.633	-18.504	-19.286	-20.668	10.66	12.82	3.56
SPK-ATZP-2012	1.850	-1.818	-13.157	17.611	16.584	2.159	-4.030	-6.130	-7.249	-14.825	-20.719	-21.639	-23.862	11.66	13.32	3.69
MARE:	1.65	2.14	13.92	15.84	16.03	2.79	4.05	6.38	7.65	18.01	21.81	22.64	24.62			
σ:	1.63	1.88	1.79	2.26	1.75	2.02	1.88	1.66	1.52	3.29	2.12	2.10	2.36			
SE:	0.36	0.42	0.40	0.50	0.39	0.45	0.42	0.37	0.34	0.74	0.47	1.93	0.53			